Available online at www.sciencedirect.com
ScienceDirect
Acta Materialia 55 (2007) 4349–4358
Acta MATERIALIA
www.elsevier.com/locate/actamat

Effect of a laser pre-quenched steel substrate surface on the crack driving force in a coating–steel substrate system

Ban-Quan Yang [a,b,c,*], Kun Zhang [b], Guang-Nan Chen [b], Geng-Xing Luo [b], Jing-Hua Xiao [b]

[a] *Division of Engineering Mechanics, Department of Mechanical Engineering, Armored Force Engineering Institute, No. 21, Du Jia Kan, Chang Xin Dian, Beijing 100072, China*
[b] *Laboratory of Surface Modification, Institute of mechanics, Chinese Academy of Sciences, No. 15, Bei Si Huan Xi Road, Beijing 100080, China*
[c] *Graduate School of the Chinese Academy of Sciences, Beijing 100080, China*

Received 21 November 2006; received in revised form 30 March 2007; accepted 1 April 2007
Available online 25 May 2007

Abstract

A mechanical model of a coating/laser pre-quenched steel substrate specimen with a crack oriented perpendicular to the interface between the coating and the hardened layer is developed to quantify the effects of the residual stress and hardness gradient on the crack driving force in terms of the *J*-integral. It is assumed that the crack tip is in the middle of the hardened layer of the pre-quenched steel substrate. Using a composite double cantilever beam model, analytical solutions can be derived, and these can be used to quantify the effects of the residual stress and the hardness gradient resulting from the pre-quenched steel substrate surface on the crack driving force. A numerical example is presented to investigate how the residual compressive stress, the coefficient linking microhardness and yield strength and the Young's modulus ratio of the hardened layer to the coating influence the crack driving force for a given crack length.

Keywords: Laser pre-quenching; Crack driving force; Residual compressive stress; Hardness gradient effect; Coating/pre-quenched steel substrate system

1. Introduction

Coating technology in combination with substrate surface pretreatment is widely used in surface engineering [1–6], such as the laser pretreatment of the steel substrate surface prior to plating a chromium coating [1], the pulsed-UV laser substrate surface pretreatment before bonding a diamond coating [2] and the excimer laser pretreatment of polymers prior to metal deposition [3]. This technology can greatly improve the mechanical properties of a coating–substrate system. Li et al. [1] stated that laser pre-quenching of a steel substrate could reduce the steep hardness gradient at the interface between the substrate and the chromium coating, and this can improve the load-bearing capacity of the material system. In fact, the total depth of the laser-quenched layer can be larger than or of the same order of magnitude as that of the thickness of the coating. Thus, the influences of the changes of the stress state and mechanical properties of the steel substrate surface due to laser pre-quenching on the fracture behavior of this material system cannot be neglected. The fracture behavior of the coating–substrate system is often a major consideration [7–18]. Smith et al. [9] stated that the typical failure mode of the coating–substrate system is often a two-stage process: in the first stage, when a coating–substrate system is under sufficient tensile stress it becomes energetically favorable for through-thickness cracks to develop in the coating; in the second stage, when the crack tip reaches the interface the crack may stop at the interface or propagate along the interface or into the substrate. Whether the crack stops or propagates depends on many factors, such as the interfacial adhesion properties between the coating

* Corresponding author.
E-mail address: yangbq1022@tom.com (B.-Q. Yang).

1359-6454/$30.00
doi:10.1016/j.actamat.2007.04.002

and the substrate, the mechanical properties of the coating and the substrate, and the load conditions [11–18].

Many researchers have studied the fracture mechanics of different elastic materials. Some classic papers have dealt with interfacial crack problems, for example, those by Williams [19] and Rice [20]. An extensive overview of the behavior of interface cracks and of cracks parallel to interfaces can be found in Hutchinson and Suo [13]. The crack at an interface may be deflected, and the criteria for such crack deflection have been derived by He and Hutchinson [21], Martinez and Gupta [22] and Lee et al. [23]. Cracks perpendicular to an interface have been investigated, for example, by Zak and Williams [24], Cook and Erdogan [25], Romeo and Ballarini [26], Schulze and Erdogan [27] and Beuth [28,29]. The most relevant results are as follows:

- when a crack approaches the interface from an elastically weaker material to a stiffer one, the (local) stress intensity decreases and reaches zero directly at the interface;
- when a crack approaches the interface from an elastically stiffer material to a weaker one, the stress intensity increases to infinity at the interface.

Chen et al. [30] have studied the applicability of the *J*-integral for such crack geometries. The case of a crack perpendicular to an interface between the coating and the substrate with its tip in the homogeneous substrate has been investigated by Ye et al. [31] and Chakravarthy et al. [32]. In this study, we investigate effects of a laser pre-quenched steel substrate surface on fracture behavior in a coating/pre-quenched steel substrate material system. Here, we deal with the case of a crack oriented perpendicular to the interface between the coating and the hardened layer, with the crack tip in the middle of the hardened layer.

Generally, laser quenching of steels can lead to two important results [33–45], one being the generation of residual compressive stress in the surface layer, which depends on the heating conditions and overlapping degree of the laser trace. Grum [33] reported that the residual compressive stress on a pre-quenched steel substrate surface and in the surface layer down to a certain depth could range between 200 and 500 MPa. The other is the change of microstructure. Shi et al. [44] stated that the grain size of the laser-hardened zone is much smaller than that of traditional quenched high-speed steels at different quenching temperatures. Liu [45] stated that a finer microstructure could be obtained by using optimum processing parameters. The changes of microstructure can lead to changes of mechanical properties, such as increases in the hardness and yield strength. Hardness, an important property, can be increased greatly, and can be measured directly or predicted by a mathematical model [46]. In general, it varies from the surface to the interior along the heat-treated track depth direction, which we call the hardness gradient effect. Also, the yield strength varies from the surface to the interior along the heat-treated track depth direction, which was called the yield strength gradient effect by Kolednik and Suresh [47,48]. Kolednik and Suresh [47,48] stated that variations in yield strength could appear in welded structures, soldered joints, nitrided or case hardened components and so on, and presented the yield stress gradient term of the crack driving force in terms of the *J*-integral.

Here, it should be emphasized that, for materials treated by laser quenching, it is very difficult to measure the yield strength for a particular point along the heat-treated track depth direction directly. Thus, it may be hard to obtain a law for the variable yield strength in a microzone from a practical viewpoint. However, the measurement of the hardness is quick and easy, and the microhardness could be approximated as three times the yield strength for metal materials under condition where the working hardening could be neglected, as stated in Tabor [49] and Ashby and Jones [50]. Recently, using dimensional analysis and finite element calculations, Cheng et al. [51] stated that the yield strength could be estimated directly from the hardness measurement in practice, and the relationship between the hardness and yield strength has been discussed in detail in Refs. [51,52]. In this work, we extend the yield strength gradient effect to the hardness gradient effect in a coating–steel substrate system, and quantify the hardness gradient and residual stress effect resulting from laser pre-quenching of the steel substrate surface on the fracture behavior of this material system based on theoretical fracture mechanics analysis. The theoretical analysis is essential to predict the crack driving force of the coating/pre-quenched steel substrate specimen, and it is also essential for the further experimental investigation of the pre-quenching effect on the fracture toughness in terms of the critical crack driving force in the coating/pre-quenched steel substrate specimen. In this work, based on small-scale yielding linear elastic fracture mechanics theory, we developed a two-dimensional mechanical model that allows us to derive analytical solutions that can be used to quantify the effects of the hardness gradient and the residual stress resulting from laser pre-quenching steel substrate surface on crack driving force in terms of *J*-integral. A numerical example is presented to investigate how the residual compressive stress, the coefficient linking microhardness and yield strength, and the Young's modulus ratio of the hardened layer to the coating influence the crack driving force for a given crack length.

2. The mechanical model

Laser quenching makes steel a more functional material as the laser quenched layer is composed of a hardened zone, a transition zone and a heat-affected zone, each zone having different properties [53]. The hardened zone is composed of a completely martensitic structure; the transition zone consists of a partly austenitized and eventually hardened structure and material fractions that did not transform to austenite during the laser irradiation; and the

heat-affected zone depends on the state of the unaffected base material [53]. However, the Young's modulus is assumed to be invariant in the four zones since general heat treatments have little influence on it in metals [54]. In this work, it should be emphasized that the laser quenching of the steel substrate occurs prior to the bonding of the coating. The laser pretreatment can be in the form of laser scanning, and the zones between the laser tracks can be overlapping zones. The laser-scanning track is assumed to be periodic for relatively large-sized flat workpieces, and the interaction between the tracks is ignored for simplicity. We can thus choose a representative track as the object of our study. We can also choose a representative track for the flat workpieces, as their surface dimension in any direction is smaller than or equal to that of the laser track. For instance, a 30CrNi2MoV steel substrate surface was laser-quenched prior to plating with a chromium coating [1], and an optical microscope image of the cross-section of the Cr coating, the laser-quenched layer and the steel substrate structure can be seen in Fig. 1. We thus developed a mechanical model of a material composed of a coating, a functional heat-treated layer and a base material, as illustrated in Fig. 2, in which h_1 and h_2 denote the thickness of the coating and the total depth of the heat-treated layer, respectively.

In this study, let x be the abscissa denoting the heat-treated track depth direction, and assume the hardness in the middle of the heat-treated track as a function of heat-treated track depth obeys the following law:

$$H = H(x), \quad x \geqslant h_1 \tag{1}$$

Hardness in the middle of the heat-treated track as a function of heat-treated track depth is illustrated in Fig. 3, in which H_m and H_0 denote the surface hardness of the quenched steel and the hardness of the base material, respectively. A numerical example of the specific law of hardness variation is given below in Section 4.

It is assumed that a crack is oriented perpendicular to the coating/hardened layer interface and that the crack tip is within the hardened layer, as illustrated in Fig. 4. The crack length a is larger than h_1 but smaller than $h_1 + h_2$.

In this work, the pre-cracked body with a constant thickness consisting of non-linear elastic material that has the same stress–strain response during the loading as an elastic–perfectly plastic material with yield strength σ_s is considered. According to the theory of elasticity and dimension analysis, if the body with a crack were linear elastic, the potential energy, Π, would depend on the exter-

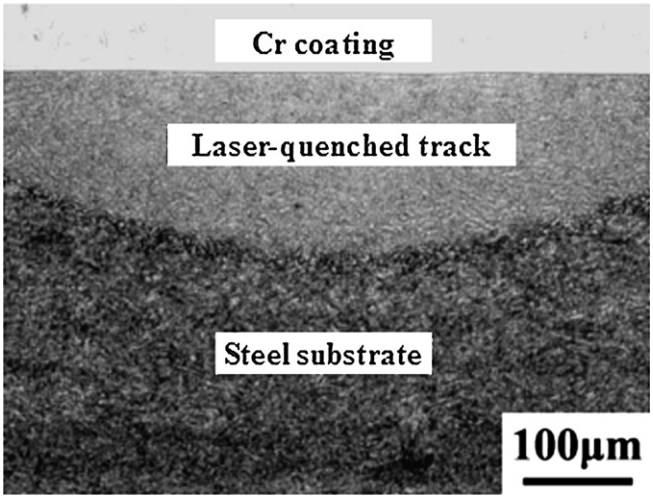

Fig. 1. Optical micrograph of a cross-section of a structure composed of Cr coating, laser-quenched layer and steel substrate (from Li et al. [1]).

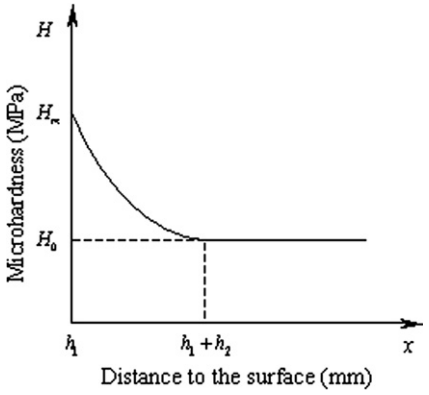

Fig. 3. Hardness in the middle of the heat-treated track as a function of the track depth.

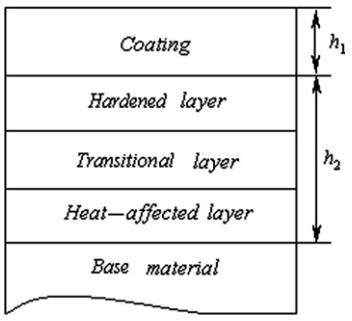

Fig. 2. A mechanical model of a material composed of a coating, a functional heat-treated layer and a base material.

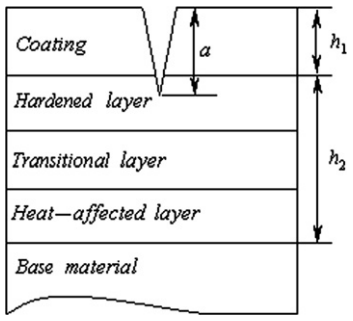

Fig. 4. A schematic illustration of the crack tip in the middle of the hardened layer.

nal load F_p, the crack length a, the Young's modulus E_1 of the coating, the Young's modulus E_2 of the laser-quenched layer (the quenched layer and the base material share the same Young's modulus) and the geometry of the body g. For our non-linear elastic body with yield stress σ_s and residual stress σ_R, the potential energy Π depends additionally on σ_s and σ_R, i.e.

$$\Pi = \Pi(F_p, a, E_1, E_2, g, \sigma_s, \sigma_R) \tag{2}$$

Cheng et al. [52] stated that indenting into an elastic–plastic solid involving a elastic–perfectly plastic solid had no analytical solution to the relationship between the mechanical properties. However, the microhardness and yield strength share the same dimension, and a relationship between them exists for a given material. So we can assume that the yield strength is a function of the microhardness, i.e.

$$\sigma_s = \sigma_s(H) \tag{3}$$

Thus Eq. (2) can be written as

$$\Pi = \Pi(F_p, a, E_1, E_2, g, \sigma_s(H), \sigma_R) \tag{4}$$

Now a thought experiment is performed: first, let the crack in the body advance by an increment Δa, while the other parameters in Eq. (4) remain constant during the crack extension. This will deduce the well-known J-integral [55]

$$J = -\frac{1}{B}\frac{\partial \Pi}{\partial a}\bigg|_{(F_p, E_1, E_2, g, \sigma_s, \sigma_R)} \tag{5}$$

which is a measure of the crack driving force. Then let the hardness increase by an increment, ΔH, while the other parameters in Eq. (4) remain constant. Now if the hardness of the body changes as the crack propagates, an additional term of the crack driving force will appear, given by

$$J_H = -\frac{1}{B}\frac{\partial \Pi}{\partial \sigma_s}\bigg|_{(F_p, a, E_1, E_2, g, \sigma_R)} \frac{d\sigma_s}{dH}\cdot\frac{dH}{da} \tag{6}$$

J_H is hereafter referred to as the hardness gradient term. The crack extension along the hardened track depth direction in combination with the hardness variation is depicted in Fig. 5, and the total crack driving force, J_{tot}, is the sum of the terms in Eqs. (5) and (6):

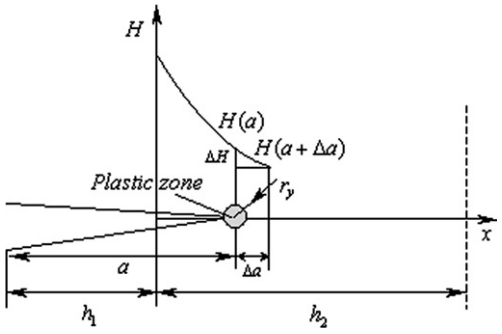

Fig. 5. A description of the crack extension in combination with hardness variation.

$$J_{tot} = J + J_H \tag{7}$$

Eq. (7) can be reduced to the case without laser pretreatment, and in this case the hardness gradient term J_H and the residual stress σ_R vanish, i.e. $dH/da = 0$, $J_H = 0$, and $\sigma_R = 0$.

3. Application of a composite double cantilever beam model

Kolednik and Suresh [47,48] and Honein and Herrmann [56] used the double cantilever beam model to obtain analytical solutions for yield strength gradient and modulus gradient problems in inhomogeneous materials, respectively. In this study, the double cantilever beam model is extended to a composite double cantilever beam model (CDCB) to study the hardness gradient effect of the heat-treated layer in combination with residual stress analysis, as shown in Fig. 6. In this work, the CDCB specimen is subjected to a pair of external loads, F_p, applied at the left end points. The residual stress, σ_R, is assumed to be a pair of external loads applied to the upper and bottom boundaries of the hardened layer of the CDCB specimen, and is compressive in the hardened layer. We assume that the crack tip lies in the middle of the hardened layer and that the length $a - h_1$ is much smaller than h_2 (the total depth of the heat-treated layer). The residual compressive stress can thus be approximated as an average value over the length $a - h_1$. When the crack length is equal to a, based on the CDCB theory, the vertical elastic displacement at the left end produced by a given load F_p is

$$\Delta_{F_p} = \frac{2F_p(a^3 - h_1^3)}{3E_2 I} + \frac{2F_p h_1^3}{3E_1 I} \tag{8}$$

The vertical elastic displacement at the left end produced by the residual compressive stress σ_R is

$$\Delta_{\sigma_R} = -\frac{\sigma_R B(a-h_1)^4}{4E_2 I} - \frac{\sigma_R B(a-h_1)^3 h_1}{3E_2 I} \tag{9}$$

where I is the moment of inertia of the cross-section of one beam and B is the constant thickness of the body. For the

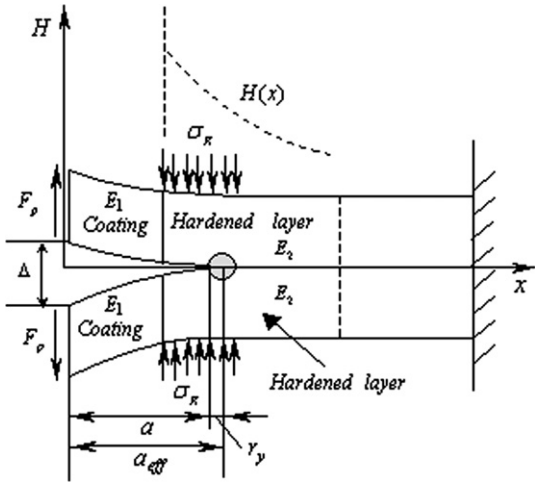

Fig. 6. A composite double cantilever beam model.

case where the residual stress is tensile, the residual stress σ_R in Eq. (9) can be replaced by $-\sigma_R$. The total vertical elastic displacement at the left end in the direction of the load F_p is the sum of the terms in Eqs. (8) and (9):

$$\Delta_e = \frac{2F_p(a^3 - h_1^3)}{3E_2I} + \frac{2F_p h_1^3}{3E_1 I} - \frac{\sigma_R B(a-h_1)^4}{4E_2 I} - \frac{\sigma_R B(a-h_1)^3 h_1}{3E_2 I} \tag{10}$$

For the small-scale yielding conditions, Irwin's [57] model of a circular plastic zone at the crack tip is adopted, and the radius is given by

$$r_y = \beta \frac{GE_2}{\sigma_s^2} \tag{11}$$

where σ_s is the yield strength at the center of the plastic zone. Note that, at a given load, σ_s determines the radius r_y of the plastic zone, and from Eq. (11) it can be seen that the radius of the circular plastic zone is inversely proportional to squared yield strength. Throughout this paper, r_y is assumed to be much smaller than the length $a - h_1$ and the body dimensions. For plane strain problems, β is a constant and is approximately equal to $1/(6\pi)$ [57]. G is the strain energy release rate, which is defined as the strain energy released per unit crack area. For the CDCB specimen, G can be calculated as

$$G = \frac{F_p^2 a^2}{BE_2 I} - \frac{F_p \sigma_R (a-h_1)^3}{2E_2 I} - \frac{F_p \sigma_R (a-h_1)^2 h_1}{2E_2 I} \tag{12}$$

The specific relationship between microhardness and yield strength can be written as [49–52]

$$\sigma_s = kH \tag{13}$$

where k is a dimensionless coefficient linking microhardness and yield strength. For a given material, the coefficient k depends on the properties of the material and can be determined by experiment [49] or finite element calculations [51,52]. In the case of the elastic–perfectly plastic metals, for most metals for which $0 < \sigma_s/E < 0.01$(E is the Young's modulus), k is between 1/2.6 and 1/2.5, as stated in Ref. [52]. For a variety of materials, k can range from 1/2.8 to 1/1.7, but for most metals for which $0 < \sigma_s/E < 0.01$ it is approximated as 1/2.8, as stated in Ref. [51]. However, Tabor [49] and Ashby and Jones [50] stated that the coefficient k could be approximated as 1/3 under the condition that the work hardening could be neglected. After using dimensional analysis and the results presented in Refs. [51,52], the hardness variation rate can represent the variation rate of the yield strength because the laser heat-treated layer and the base material share the same Young's modulus and the nonlinear elastic material is assumed to be elastic–perfectly plastic in this work. Substituting Eq. (13) into Eq. (11) yields

$$r_y = \beta \frac{GE_2}{k^2 H^2} \tag{14}$$

Including the displacement contributed by perfect plasticity, a good estimate of the total displacement at the left end in the direction of the load F_p can be obtained by replacing the crack length in Eq. (10) by the effective crack length, $a_{eff} = a + r_y$, i.e.

$$\Delta = \frac{2F_p a^3}{3E_2 I}\left[\left(1+\frac{r_y}{a}\right)^3 - \left(\frac{h_1}{a}\right)^3\right] + \frac{2F_p h_1^3}{3E_1 I} - \frac{\sigma_R B a^4}{4E_2 I}\left(1+\frac{r_y}{a}-\frac{h_1}{a}\right)^4 - \frac{\sigma_R B a^3 h_1}{3E_2 I}\left(1+\frac{r_y}{a}-\frac{h_1}{a}\right)^3 \tag{15}$$

Thus, the total displacement Δ at the left end in the direction of the load F_p, which is composed of the displacements contributed by the load F_p, the residual stress σ_R and the perfect plasticity, is obtained. As was pointed out by Rice [58], the potential energy for a load-controlled test, $\Pi|_{F_p}$, can be calculated from

$$\Pi|_{F_p} = -\int_0^{F_p} \Delta \mathrm{d}F_p \tag{16}$$

Using Eqs. (12) and (14), the specific potential energy expression can be obtained by substituting Eq. (15) into Eq. (16):

$$\Pi|_{F_p} = \sum_{i=1}^{9} C_i F_p^i \tag{17}$$

where values of $C_i (i = 1, 2, 3, \ldots, 9)$ are given in Appendix A.

Eq. (17), together with Eqs. (5)–(7), leads to the desired analytical solutions:

$$J = \sum_{i=1}^{11} A_i a^i \tag{18}$$

$$J_H = \sum_{i=1}^{4} \lambda_{-(2i+1)} H^{-(2i+1)} \frac{\mathrm{d}H}{\mathrm{d}x} \tag{19}$$

$$J_{tot} = J + J_H = \sum_{i=1}^{11} A_i a^i + \sum_{i=1}^{4} \lambda_{-(2i+1)} H^{-(2i+1)} \frac{\mathrm{d}H}{\mathrm{d}x} \tag{20}$$

where values of A_i ($i = 1, 2, 3, \ldots, 11$) are given in Appendix B and $\lambda_{-(2i+1)} (i = 1, 2, 3, 4)$ are given in Appendix C.

Eq. (18) is the term of the crack driving force that includes the residual stress, and Eq. (19) is the other term of the crack driving force that includes the hardness gradient. Thus, the total crack driving force expressed in Eq. (20), which is the sum of the two terms, is obtained.

4. A numerical example

A numerical example will assess the influences of the variations of the residual compressive stress, the coefficient linking microhardness and yield strength, and the Young's modulus ratio of the hardened layer to the coating on the crack driving force for a given crack length. The hardness gradient in the middle of the heat-treated track depth direction x is assumed to follow an exponential function

$$H(x) = D_0 \exp[\delta(x - h_1)], \quad x \geqslant h_1 \tag{21}$$

where D_0 and δ are the constants to be determined. From Fig. 3, it can be seen when $x = h_1$, $H = H_m = D_0$. When $x = h_1 + h_2$, $H = H_0 = D_0 \exp(\delta h_2)$. Once the hardness values at the two points are known, the constants D_0 and δ can be determined. For a particular case, one of the hardness distribution characteristics in the middle of the heat-treated track along the heat-treated track depth direction is taken from Ref. [59], in which, when $x = h_1$, H is approximately equal to 8×10^9 Pa, and when $x = h_1 + h_2$, H is approximately equal to 3×10^9 Pa. h_2 is the total depth of the heat-treated layer and is approximately equal to 0.6 mm [59]. Using Eq. (21), D_0 and δ can be determined, and the corresponding hardness variation law is given as

$$H(x) = 8.0 \times 10^9 \exp[-1634.7(x - h_1)], \quad x \geqslant h_1 \tag{22}$$

Some parameters used for the calculations of J, J_H and J_{tot} are given in Table 1. All the parameters in Table 1 are invariant throughout the following calculations. For the first calculation, the value of the residual compressive stress σ_R is assumed to be 200 MPa. k is assumed to be 1/2.5 [52]. The Young's modulus E_1 of the coating is assumed to be 290 GPa, and the Young's modulus E_2 of the hardened layer is assumed to be 210 GPa. Given these conditions, J_{tot} can be calculated to be 1.3514×10^3 (J/m^2). It should be emphasized that this value is also a normalized factor for the following analysis.

In this work, we investigate the influence of the variation of the residual compressive stress on the crack driving force. Here, we let σ_R be normalized with respect to the constant σ, and $\sigma = F_p/[B(a - h_1)]$. In this calculation, $k = 1/2.5$, $E_1 = 290$ GPa and $E_2 = 210$ GPa. Let J^R_{tot} denote the crack driving force of different residual compressive stresses and be normalized with respect to J_{tot}, as mentioned above. The plot of the ratio J^R_{tot}/J_{tot} vs. the ratio σ_R/σ is shown in Fig. 7.

For convenience, we define another dimensionless coefficient, k', which is equal to $1/k$. In this work, based on the results presented in Refs. [49–52], the coefficient k' is assumed to range from 1.7 to 3.0. In this calculation, $\sigma_R = 200$ MPa, $E_1 = 290$ GPa and $E_2 = 210$ GPa. Let $J^{k'}_{tot}$ denote the crack driving force of different coefficients and be normalized with respect to J_{tot}. The plot of the ratio $J^{k'}_{tot}/J_{tot}$ vs. the coefficient k' is shown in Fig. 8.

In the following, we investigate the Young's modulus ratio E_2/E_1 on the crack driving force. In this calculation, $\sigma_R = 200$ MPa, $k = 1/2.5$, and $E_1 = 290$ GPa. Let J^E_{tot} denote the crack driving force of different modulus ratios and be normalized with respect to J_{tot}. The plot of the ratio J^E_{tot} vs. the modulus ratio E_2/E_1 is shown in Fig. 9.

Table 1
Some parameters used for the calculations

F_p (N)	h_1 (μm)	h_2 (μm)	a (μm)	B (μm)	I (mm^4)	β
0.15	50	600	100	20	1.33×10^{-8}	$1/(6\pi)$

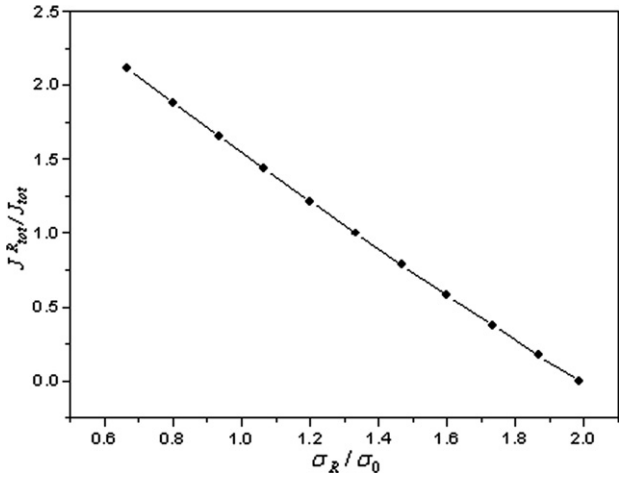

Fig. 7. Plot of the ratio J^R_{tot}/J_{tot} vs. the ratio σ_R/σ_0, $\sigma_0 = F_p/(B(a - h_1))$.

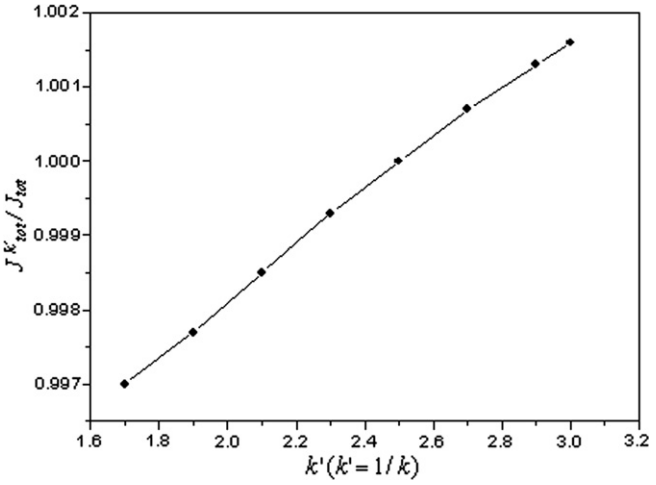

Fig. 8. Plot of the ratio $J^{k'}_{tot}/J_{tot}$ vs. the coefficient k' ($k' = 1/k$).

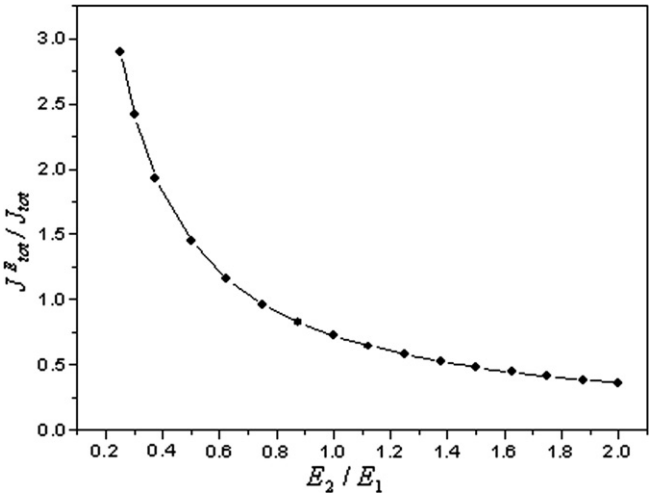

Fig. 9. Plot of the ratio J^E_{tot}/J_{tot} vs. the Young's modulus ratio E_2/E_1.

5. Results and discussions

From Fig. 7, it can be seen that the crack driving force decreases significantly with increasing residual compressive

stress. In contrast, if the residual stress is tensile, the crack driving force will greatly increase with increasing residual tensile stress, and it will adversely facilitate the crack propagation. This case can be detrimental to the workpieces.

From Fig. 8, it can be seen that the crack driving force increases as k' increases. This can be explained in the following way. Apart from the case where the variation of k' can represent a variety of materials, the increase in k' from 1.7 to 3 also implies the decrease in the yield strength from another standpoint in that the hardness is invariant for a given crack length during this calculation. So, it is reasonable to assume that the increase in k' or the decrease in the yield strength leads to the increase in the crack driving force.

From Fig. 9, it can be seen that the crack driving force decreases as the modulus ratio E_2/E_1 increases. For a given Young's modulus E_1 of the coating, the increase in the modulus ratio E_2/E_1 causes an increase in the Young's modulus E_2 of the hardened layer. From Eq. (12), it can be seen that the crack driving force tends to decrease as the Young's modulus of the hardened layer increases.

So, from the analysis of Figs. 7–9, we can see that the higher residual compressive stress, higher yield strength and higher Young's modulus ratio of the hardened layer to the coating can greatly decrease the crack driving force. The decrease in the crack driving force means an increase in the resistance to crack growth, and this situation can improve the fracture behavior or improve the load-bearing capacity of the material. In addition to the results presented in this work, the high residual compressive stress and high strength resulting from laser heat treatment also play an important role in improving fatigue behavior [39–41], such as the decrease in the fatigue crack growth rate or the increase in resistance to crack growth. In addition, if the variation law and magnitude of the residual stress can be determined, the procedure presented in this paper can be used to study the pre-quenched effect on fracture toughness of this material system.

In order to obtain accurate results throughout the calculation, it should be noticed that the geometric parameters of the specimen must satisfy the composite beam model, and the radius r_y of the circular plastic zone at the crack tip must satisfy the condition that it is much smaller than the length $a - h_1$ and specimen dimensions. The plastic zone size r_y depends on the load condition and the mechanical properties of the specimen, and different load conditions and mechanical properties of the specimen may lead to different plastic zone sizes. So, the condition that r_y is much smaller than the length $a - h_1$ and the specimen dimensions will not always be fulfilled in the numerical example, and we should choose a proper load parameter to satisfy it according to the given conditions, including the yield strength of the specimen, the crack length and the specimen dimensions. This limitation of the model affects its applicability to practical cases. For example, if we want to measure the fracture toughness of a specimen, we should reasonably estimate the fracture toughness and plastic zone size r_y prior to the experiment, and then design the proper load conditions, the length $a - h_1$ and the specimen dimensions. Materials with high yield strength and low fracture toughness may exhibit small-scale yielding fracture, and the plastic zone size may naturally satisfy this condition. For materials with low yield strength and high fracture toughness, we should choose a plane strain specimen (thick specimen) in that the plane strain condition can reduce plastic deformation prior to crack extension, and the condition that r_y is much smaller than the length $a - h_1$ and specimen dimensions will be satisfied. If the specimen exhibits large-scale plastic deformation prior to crack extension during the experiment, the results presented in this paper will be unsuitable in that the large-scale plastic deformation could dissipate much potential energy, and we should use the elastic–plastic fracture mechanics to deal with the problem. At the same time, the magnitude of the external load F_p, which is a constant for this calculation, must also be properly taken in that the total displacement Δ and the elastic strain energy release rate G must be positive, otherwise it would be a crack closure/contact problem.

The results obtained from the mechanical model are based on a number of assumptions. The crack tip is assumed to be in the middle of the hardened layer, and the length $a - h_1$ is much smaller than the total depth of the heat-treated layer. So the residual compressive stress can be approximated as an average value over the length $a - h_1$. The cases in which the crack tip is in the hardened layer, the transitional layer, the heat-affected layer or the base material are different, and must be dealt with separately. For example, if the crack tip is in either the transitional layer or the heat-affected layer, we must consider the residual stress gradient effect, i.e. the residual stress as a function of the depth below the surface, or the variation of the residual stress from compressive to tensile [33–35]. So the results presented in this paper are suitable for the case where the crack tip is in the middle of the hardened layer. The hardness in the middle of the heat-treated track as a function of the heat-treated track depth is assumed to satisfy an exponentially decaying law. One can also take other formulas to approximately express the law of the hardness variation along the heat-treated track depth direction for a specific or practical case.

The results presented in this work are not only limited to the case of laser pretreatment, but can also be extended to other forms of high-energy surface pretreatments, such as electron beam surface pretreatment and ion beam surface pretreatment. The differences are that the magnitude and the distribution laws of the hardness and residual stress may be different for corresponding specific cases. Once the specific laws and magnitude of the residual stress and hardness are given, the procedure presented in this paper can also be adopted without any difficulty.

In this work, if we let $h_1 = 0$ and $E_1 = 0$, the mechanical model presented in this paper can be reduced to the mechanical model presented in Ref. [60], in which it was

developed to quantify the effect resulting from laser quenching on the crack driving force in a laser-quenched steel specimen without a coating.

This paper deals with the pre-quenched effect on the fracture behavior of a crack that is oriented perpendicular to the interface between the coating and the hardened layer. Since Li et al. [1] reported that laser quenching a steel substrate prior to bonding the coating has an extremely large effect on the morphologies and microstructure of the substrate/coating interface, it should be pointed out that the investigation of the pre-quenched effect on the interfacial fracture behavior or interfacial adhesion properties between the coating and the hardened layer in this material system is also promising, and the results will be reported later.

6. Conclusions

The mechanical model presented in this paper allows us to derive analytical solutions that can be used to quantify the effect of laser pre-quenching on the fracture behavior in a coating/pre-quenched steel substrate system. The analytical solutions obtained from this mechanical model can not only be used as a means to predict the crack driving force of the coating/pre-quenched steel substrate system, but also serve as a baseline for further experimental investigation of the fracture toughness of this material system, accounting for the laser pre-quenched effect. For a given crack length, the numerical example shows that the crack driving force decreases with increasing residual compressive stress, yield strength or (and) Young's modulus of the hardened layer.

The results presented in this work can also be applied to other forms of high-energy surface pretreatments of the steel substrate surface prior to bonding the coating.

Acknowledgements

The financial support provided by the National Natural Science Foundation of China (Grant No. 50531060, 50471087) is greatly acknowledged.

Appendix A

$$\Pi|_{F_p} = \sum_{i=1}^{9} C_i F_p^i = C_1F_p + C_2F_p^2 + C_3F_p^3 + C_4F_p^4 + C_5F_p^5 + C_6F_p^6 + C_7F_p^7 + C_8F_p^8 + C_9F_p^9.$$

$$C_1 = \frac{\sigma_R B h_1}{3E_2 I}(a-h_1)^3 + \frac{\sigma_R B}{4E_2 I}(a-h_1)^4,$$

$$C_2 = -\frac{h_1^3}{3E_1 I} - \frac{a^3-h_1^3}{3E_2 I} - \frac{a^2 B\beta\sigma_R^2(a-h_1)^4}{4E_2 I^2 k^2 H^2},$$

$$C_3 = \frac{2a^3\sigma_R\beta(a-h_1)^2}{3E_2 I^2 k^2 H^2} + \frac{Ba^2\beta^2\sigma_R^3(a-h_1)^5(3a-h_1)}{24E_2 I^3 k^4 H^4},$$

$$C_4 = -\frac{\beta a^4}{2E_2 B I^2 k^2 H^2} - \frac{\beta^2 a^3\sigma_R^2(a-h_1)^3(2a-h_1)}{4E_2 I^3 k^4 H^4} - \frac{\beta^3 a^3 B\sigma_R^4(a-h_1)^6(3a-2h_1)}{96E_2 I^4 k^6 H^6},$$

$$C_5 = \frac{a^4\beta^2\sigma_R(a-h_1)(2a-h_1)}{5E_2 B I^3 k^4 H^4} + \frac{\beta^3 a^3\sigma_R^3(a-h_1)^6}{60E_2 I^4 k^6 H^6} + \frac{a^4\beta^3\sigma_R^3(a-h_1)^4 h_1}{20E_2 I^4 k^6 H^6} + \frac{\sigma_R B a^4}{20E_2 I}\left\{\frac{2\beta^2(a-h_1)^2}{B^2 I^2 k^4 H^4} + \frac{2\beta^3\sigma_R^2(a-h_1)^5}{BI^3 k^6 H^6} + \left[\frac{\beta^2\sigma_R^2(a-h_1)^4}{4I^2 k^4 H^4} + \frac{2\beta(a-h_1)}{BIk^2 H^2}\right]^2\right\},$$

$$C_6 = -\frac{\beta^2 a^5}{3E_2 B^2 I^3 k^4 H^4} - \frac{\beta^4 a^5\sigma_R^4(a-h_1)^6}{48E_2 I^5 k^8 H^8} - \frac{\beta^3 a^4\sigma_R^2(a-h_1)^4}{12E_2 B I^4 k^6 H^6} - \frac{\beta^3 a^5\sigma_R^2(a-h_1)^2(3a-2h_1)}{12BE_2 I^4 k^6 H^6},$$

$$C_7 = \frac{\beta^3\sigma_R a^6 h_1}{21E_2 B^2 I^4 k^6 H^6} + \frac{\sigma_R\beta^3 a^5(a-h_1)(2a+h_1)}{7E_2 B^2 I^4 k^6 H^6} + \frac{3\beta^4 a^6\sigma_R^3(a-h_1)^4}{56E_2 B I^5 k^8 H^8},$$

$$C_8 = -\frac{\beta^4 a^7\sigma_R^2(a-h_1)^2}{16B^2 E_2 I^5 k^8 H^8} - \frac{\beta^3 a^6}{12E_2 B^3 I^4 k^6 H^6},$$

$$C_9 = \frac{\beta^4\sigma_R a^8}{36E_2 B^3 I^5 k^8 H^8}.$$

Appendix B

$$J = \sum_{i=1}^{11} A_i a^i = A_1a + A_2a^2 + A_3a^3 + A_4a^4 + A_5a^5 + A_6a^6 + A_7a^7 + A_8a^8 + A_9a^9 + A_{10}a^{10} + A_{11}a^{11}.$$

$$A_1 = \frac{\sigma_R^2 h_1^4\beta F_p^2}{2E_2 I^2 k^2 H^2} - \frac{\sigma_R h_1^2 F_p}{E_2 I} - \frac{\beta^2\sigma_R^3 h_1^6 F_p^3}{12E_2 I^3 k^4 H^4},$$

$$A_2 = \frac{F_p(2\sigma_R B h_1 + F_p)}{E_2 BI} - \frac{\beta^3\sigma_R^3 h_1^6 F_p^4(4F_p + 5B\sigma_R h_1)}{80E_2 BI^4 k^6 H^6} - \frac{\beta\sigma_R h_1^2 F_p^2(3\sigma_R B h_1 + 2F_p)}{E_2 BI^2 k^2 H^2} + \frac{\beta^2 h_1^4\sigma_R^2 F_p^3(3F_p - 11\sigma_R B h_1)}{4E_2 BI^3 k^4 H^4},$$

$$A_3 = \frac{6\beta\sigma_R^2 h_1^2 F_p^2}{E_2 I^2 k^2 H^2} + \frac{16\beta\sigma_R h_1 F_p^3}{3E_2 BI^2 k^2 H^2} - \frac{5\beta^2\sigma_R^2 h_1^3 F_p^4}{E_2 BI^3 k^4 H^4} - \frac{25\beta^2\sigma_R^3 h_1^4 F_p^3}{6E_2 I^3 k^4 H^4} + \frac{2\beta F_p^4}{E_2 B^2 I^2 k^2 H^2} - \frac{\sigma_R F_p}{E_2 I} + \frac{5\beta^3\sigma_R^4 h_1^6 F_p^4}{8E_2 I^4 k^6 H^6} + \frac{4\beta^3\sigma_R^3 h_1^5 F_p^5}{5E_2 BI^4 k^6 H^6} + \frac{\beta^3\sigma_R^2 h_1^4 F_p^6}{3E_2 B^2 I^4 k^6 H^6} - \frac{2\beta^2\sigma_R h_1^2 F_p^5}{E_2 B^2 I^3 k^4 H^4} - \frac{\beta^4\sigma_R^5 h_1^8 F_p^5}{80E_2 I^5 k^8 H^8},$$

$$A_4 = \frac{45\beta^2\sigma_R^2 h_1^2 F_p^4}{4E_2BI^3k^4H^4} - \frac{5\beta^3\sigma_R^4 h_1^5 F_p^4}{2E_2I^4k^6H^6} - \frac{5\beta^3\sigma_R^2 h_1^3 F_p^6}{2E_2B^2I^4k^6H^6} + \frac{5\beta^4\sigma_R^4 h_1^6 F_p^6}{48E_2BI^5k^8H^8} + \frac{5\beta^2 F_p^6}{3E_2B^3I^3k^4H^4} - \frac{4\beta^3\sigma_R^3 h_1^4 F_p^5}{E_2BI^4k^6H^6} + \frac{6\beta^2\sigma_R h_1 F_p^5}{E_2B^2I^3k^4H^4} + \frac{\beta^4\sigma_R^5 h_1^7 F_p^5}{8E_2I^5k^8H^8} + \frac{25\beta^2\sigma_R^3 h_1^3 F_p^3}{3E_2I^3k^4H^4} - \frac{10\sigma_R\beta F_p^3}{3E_2BI^2k^2H^2} - \frac{5\beta^3\sigma_R h_1^2 F_p^7}{7E_2B^3I^4k^6H^6} - \frac{5\beta\sigma_R^2 h_1 F_p^2}{E_2I^2k^2H^2},$$

$$A_5 = \frac{\beta^3 F_p^8}{2E_2B^4I^4k^6H^6} - \frac{35\beta^2\sigma_R^3 h_1^2 F_p^3}{4E_2I^3k^4H^4} + \frac{13\beta^3\sigma_R^2 h_1^2 F_p^6}{2E_2B^2I^4k^6H^6} - \frac{3\beta^4\sigma_R^4 h_1^5 F_p^6}{4E_2BI^5k^8H^8} + \frac{85\beta^3\sigma_R^4 h_1^4 F_p^4}{16E_2I^4k^6H^6} - \frac{21\beta^2\sigma_R^2 h_1 F_p^4}{2E_2BI^3k^4H^4} - \frac{21\beta^2\sigma_R F_p^5}{5E_2B^2I^3k^4H^4} + \frac{46\beta^3\sigma_R^3 h_1^3 F_p^5}{5E_2BI^4k^6H^6} - \frac{21\beta^4\sigma_R^5 h_1^6 F_p^5}{40E_2I^5k^8H^8} + \frac{16\beta^3\sigma_R h_1 F_p^7}{7E_2B^3I^4k^6H^6} - \frac{9\beta^4\sigma_R^3 h_1^4 F_p^7}{28E_2B^2I^5k^8H^8},$$

$$A_6 = \frac{7\beta^4\sigma_R^2 h_1^2 F_p^8}{16B^3E_2I^5k^8H^8} - \frac{217\beta^3\sigma_R^3 h_1^2 F_p^5}{20E_2BI^4k^6H^6} + \frac{49\beta^4\sigma_R^5 h_1^5 F_p^5}{40E_2I^5k^8H^8} + \frac{14\beta^2\sigma_R^3 h_1 F_p^3}{3E_2I^3k^4H^4} - \frac{2\beta^3\sigma_R F_p^7}{E_2B^3I^4k^6H^6} + \frac{3\beta^4\sigma_R^3 h_1^3 F_p^7}{2E_2B^2I^5k^8H^8} + \frac{35\beta^4\sigma_R^4 h_1^4 F_p^6}{16E_2BI^5k^8H^8} - \frac{7\beta^3\sigma_R^2 h_1 F_p^6}{E_2B^2I^4k^6H^6} + \frac{7\beta^2\sigma_R^2 F_p^4}{2E_2BI^3k^4H^4} - \frac{105\beta^3\sigma_R^4 h_1^3 F_p^4}{16E_2I^4k^6H^6},$$

$$A_7 = -\frac{2\sigma_R\beta^4 F_p^9}{9E_2B^4I^5k^8H^8} + \frac{19\sigma_R^4\beta^3 h_1^2 F_p^4}{4E_2I^4k^6H^6} - \frac{\sigma_R^2\beta^4 h_1 F_p^8}{E_2B^3I^5k^8H^8} - \frac{18\sigma_R^3\beta^4 h_1^2 F_p^7}{7E_2B^2I^5k^8H^8} - \frac{\sigma_R^3\beta^2 F_p^3}{E_2I^3k^4H^4} + \frac{32\sigma_R^3\beta^3 h_1 F_p^5}{5E_2BI^4k^6H^6} - \frac{7\beta^4\sigma_R^5 h_1^4 F_p^5}{4E_2I^5k^8H^8} + \frac{8\beta^3\sigma_R^2 F_p^6}{3E_2B^2I^4k^6H^6} - \frac{10\sigma_R^4\beta^4 h_1^3 F_p^6}{3E_2BI^5k^8H^8},$$

$$A_8 = \frac{27\beta^4\sigma_R^3 F_p^7 h_1}{14E_2B^2I^5k^8H^8} + \frac{9\beta^4\sigma_R^2 F_p^8}{16E_2B^3I^5k^8H^8} - \frac{15\beta^3\sigma_R^4 F_p^4 h_1}{8E_2I^4k^6H^6} + \frac{45\beta^4\sigma_R^4 F_p^6 h_1^2}{16E_2BI^5k^8H^8} + \frac{63\beta^4\sigma_R^5 F_p^5 h_1^3}{40E_2I^5k^8H^8} - \frac{3\beta^3\sigma_R^3 F_p^5}{2E_2BI^4k^6H^6},$$

$$A_9 = \frac{5\sigma_R^4\beta^3 F_p^4}{16E_2I^4k^6H^6} - \frac{15\sigma_R^3\beta^4 F_p^7}{28E_2B^2I^5k^8H^8} - \frac{5\sigma_R^4\beta^4 h_1 F_p^6}{4E_2BI^5k^8H^8} - \frac{7\sigma_R^5\beta^4 h_1^2 F_p^5}{8E_2I^5k^8H^8},$$

$$A_{10} = \frac{11\sigma_R^4\beta^4 F_p^6}{48E_2BI^5k^8H^8} + \frac{11\sigma_R^5\beta^4 h_1 F_p^5}{40E_2I^5k^8H^8},$$

$$A_{11} = -\frac{3\beta^4\sigma_R^5 F_p^5}{80E_2I^5k^8H^8}.$$

Appendix C

$$J_H = \sum_{i=1}^{4}\lambda_{-(2i+1)}H^{-(2i+1)}\frac{dH}{dx} = (\lambda_{-3}H^{-3} + \lambda_{-5}H^{-5} + \lambda_{-7}H^{-7} + \lambda_{-9}H^{-9})\frac{dH}{dx}.$$

$$\lambda_{-3} = \frac{4\beta\sigma_R F_p^3 a^2(a-h_1)^2 h_1}{3BE_2I^2k^2} - \frac{a^4\beta F_p^4}{E_2B^2I^2k^2} - \frac{\beta a^2\sigma_R^2 F_p^2(a-h_1)^4}{2E_2I^2k^2},$$

$$\lambda_{-5} = \frac{2\sigma_R\beta^2 a^4 F_p^5(a-h_1)(7a-5h_1)}{5E_2B^2I^3k^4} - \frac{4\beta^2 a^5 F_p^6}{3E_2B^3I^3k^4} - \frac{\beta^2 a^3\sigma_R^2 F_p^4(a-h_1)^3(2a-h_1)}{E_2BI^3k^4} + \frac{\beta^2 a^2\sigma_R^3 F_p^3(a-h_1)^5(3a-h_1)}{6E_2k^4I^3},$$

$$\lambda_{-7} = \frac{\beta^3 a^3\sigma_R^3 F_p^5(a-h_1)^6}{10E_2BI^4k^6} - \frac{\beta^3 a^6 F_p^8}{2E_2B^4I^4k^6} - \frac{\beta^3 a^5\sigma_R^2 F_p^6(a-h_1)^2(3a-2h_1)}{2E_2B^2I^4k^6} - \frac{\beta^3 a^4\sigma_R^2 F_p^6(a-h_1)^4}{2E_2B^2I^4k^6} - \frac{\beta^3 a^3\sigma_R^4 F_p^4(a-h_1)^6(3a-2h_1)}{16E_2I^4k^6} + \frac{2\beta^3 a^6\sigma_R h_1 F_p^7}{7E_2B^3I^4k^6} + \frac{6\beta^3 a^5\sigma_R F_p^7(a-h_1)(2a-h_1)}{7E_2B^3I^4k^6} + \frac{3\beta^3 a^4\sigma_R^3 F_p^5(a-h_1)^4(3a-2h_1)}{10E_2BI^4k^6},$$

$$\lambda_{-9} = \frac{2\beta^4 a^8\sigma_R F_p^9}{9E_2B^4I^5k^8} - \frac{\beta^4 a^7\sigma_R^2 F_p^8(a-h_1)^2}{2E_2B^3I^5k^8} + \frac{3\beta^4 a^6\sigma_R^3 F_p^7(a-h_1)^4}{7E_2B^2I^5k^8} + \frac{\beta^4 a^4\sigma_R^5 F_p^5(a-h_1)^8}{40E_2I^5k^8} - \frac{\beta^4 a^5\sigma_R^4 F_p^6(a-h_1)^6}{6BE_2I^5k^8}.$$

References

[1] Li HX, Chen GN, Zhang GX, Zhang K, Luo GX. Surf Coat Technol 2006;201:902.

[2] Li TJ, Lou QH, Dong JX, Wei YR, Zhou J, Liu JR, et al. Appl Surf Sci 2002;193:102.

[3] Horn H, Beil S, Wesner DA, Weichenhain R, Kreutz EW. Nucl Instrum Methods Phys Res Sect B: Beam Interactions with Materials and Atoms 1999;151:279.

[4] Weichenhain R, Wesner DA, Pfleging W, Horn H, Kreutz EW. Appl Surf Sci 1997;109–110:264.

[5] Guzman L, Miotello A, Checchetto R, Adami M. Surf Coat Technol 2002;158–159:558.

[6] Frerichs H, Stricker J, Wesner DA, Kreutz EW. Appl Surf Sci 1995;86:405.

[7] Li MH, Sun XF, Hu WY, Guan HR. Surf Coat Technol 2006;200:3770.
[8] Zhou YC, Tonomori T, Yoshida A, Liu L, Bignall G, Hashida T. Surf Coat Technol 2002;157:118.
[9] Smith GA, Jennett N, Housden J. Surf Coat Technol 2005;197:336.
[10] Ma XQ, Cho S, Takemoto M. Surf Coat Technol 2001;139:55.
[11] Hu MS, Evans AG. Acta Metall 1989;37:917.
[12] Wei R, Wilbur PJ, Kustas FM. J Tribol Trans ASME 1992;114:298.
[13] Hutchinson JW, Suo Z. Adv Appl Mech 1992;29:63.
[14] Blanpain B, Celis JP, Roos JR, Ebberink J, Smeets J. Thin Solid Films 1993;223:65.
[15] Grill A, Patel V. Diam Relat Mater 1993;2:597.
[16] Wang JS, Sugimura Y, Evans AG, Tredway WK. Thin Solid Films 1998;325:163.
[17] Volinsky AA, Moody NR, Gerberich WW. Acta Mater 2002;50:441.
[18] Xie CJ, Wei T. Acta Mater 2005;53:477.
[19] Williams ML. Bull Seismol Soc Am 1959;49:199.
[20] Rice JR. J Appl Mech 1988;55:98.
[21] He MY, Hutchinson JW. Int J Solids Struct 1989;25:1053.
[22] Martinez D, Gupta V. J Mech Phys Solids 1994;42:1242.
[23] Lee W, Howard J, Clegg WJ. Acta Mater 1996;44:3905.
[24] Zak AR, Williams ML. J Appl Mech 1963;30:142.
[25] Cook TS, Erdogan F. Int J Eng Sci 1972;10:667.
[26] Romeo A, Ballarini R. J Appl Mech 1995;62:614.
[27] Schulze GW, Erdogan F. Int J Solids Struct 1998;35:3615.
[28] Beuth JL. Int J Solids Struct 1992;29:1657.
[29] Beuth JL, Klingbeil NW. J Mech Phys Solid 1996;44:1411.
[30] Chen WH, Chen KT, Chiang CR. Eng Fract Mech 1988;30:13.
[31] Ye T, Suo Z, Evans AG. Int J Solids Struct 1992;29:2639.
[32] Chakravarthy SS, Jordan EH, Chiu WKS. Eng Fract Mech 2005;72:1286.
[33] Grum J, Žerovnik P. Heat Treat 1993;25:32.
[34] Grum J. In: Totten GE, Funatani K, Xie L, editors. Handbook of Metallurgical Process Design. New York: Marcel Dekker; 2004. p. 641.
[35] Grum J, Sturm R, Žerovnik P. Proceedings of the 2nd International Conference on Quenching and the Control of Distortion, Cleveland, OH, 4–7 November 1996. p. 181.
[36] Suresh S, Giannakopoulos AE. Acta Mater 1998;46:5755.
[37] Heitkemper M, Bohne C, Pyzalla A, Fischer A. Int J Fatigue 2003;25:101.
[38] Merrien P, Lieurade HP, Theobalt M, Baudry G, Puig T, Leroy F. Surf Eng 1992;8:61.
[39] De la Cruz Pedro, Odén Magnus, Ericsson Torsten. Int J Fatigue 1998;20:389.
[40] Doong JL, Chen TJ, Tan YH. Eng Fract Mech 1989;33:483.
[41] Tsay LW, Young MC, Chen C. Corros Sci 2003;45:1985.
[42] Kato A. J Eng Mater Technol 1985;107:195.
[43] Singh HB, Copley SM, Bass M. Metall Trans 1981;12A:138.
[44] Shi GQ, Ding PD, Liu JL, Yin HJ, Wang J. Acta Metall Mater 1995;43:217.
[45] Liu QB, Liu H. J Mater Process Technol 1999;88:77.
[46] Guan YH, Chen TL, Wang HG, Zhang JT. J Mater Process Technol 1997;63:614.
[47] Kolednik O, Suresh S. Mater Sci Forum 1999;308–311:963.
[48] Kolednik O. Int J Solids Struct 2000;37:781.
[49] Tabor D. The Hardness of Metals. London: Oxford University Press; 1951.
[50] Ashby MF, Jones DRH. Engineering Materials. London: Pergamon Press; 1980. p. 105.
[51] Cheng YT, Cheng CM. J Appl Phys 1998;84:1284.
[52] Cheng YT, Cheng CM. Int J Solids Struct 1999;36:1231.
[53] Obergfell K, Schulze V, Vöhringer O. Mater Sci Eng A 2003;355:348.
[54] Meyers MA, Chawla KK. Mechanical Metallurgy. Englewood Cliffs, NJ: Prentice Hall; 1984.
[55] Rice JR. In: Liebowitz H, editor. Fracture: An Advanced Treatise. New York: Academic Press; 1968. p. 191.
[56] Honein T, Herrmann G. J Mech Phys Solids 1997;45:789.
[57] Irwin GR. In: Proceedings of the seventh sagamore ordance materials conference IV. New York: Syracus University; 1960. p. 63.
[58] Rice JR. J Appl Mech 1968;35:379.
[59] Lo KH, Cheng FT, Man HC. Surf Coat Technol 2003;173:96.
[60] Yang BQ, Zhang K, Chen GN, Luo GX, Xiao JH. Surf Coat Technol 2006;201:2208.